

# Evidence of cascaded emission in a dual-wavelength quantum cascade laser

Kale J. Franz,<sup>a)</sup> Daniel Wasserman, Anthony J. Hoffman, David C. Jangraw, Kuen-Ting Shiu,<sup>b)</sup> Stephen R. Forrest,<sup>b)</sup> and Claire Gmachl

Department of Electrical Engineering, Princeton University, Princeton, New Jersey 08544

(Received 20 December 2006; accepted 24 January 2007; published online 28 February 2007)

This letter reports on a quantum cascade laser that exhibits simultaneous dual-wavelength emission from two consecutive optical transitions in each active region. These “cascaded” transitions—a second-excited state to first-excited state and a first-excited state to ground state—yield light at  $\sim 9.5$  and  $\sim 8.2$   $\mu\text{m}$ , respectively, in good agreement with simulations. The two lasing wavelengths have similar thresholds at the leading edge of a current pulse. © 2007 American Institute of Physics. [DOI: 10.1063/1.2709970]

The core concept central to the quantum cascade (QC) laser of precisely engineered coupled quantum wells lends itself to extreme flexibility in implementing innovative device design strategies.<sup>1</sup> Since initially demonstrated in 1994,<sup>2</sup> there have been numerous examples of QC lasers that extend conceptually beyond the traditional four-level laser system.<sup>1</sup> Many of these designs have turned the QC laser into multi-wavelength emitters. For example, superlattice QC lasers have been made for multiwavelength operation.<sup>3</sup> Using QC active regions as both an optical pump and a nonlinear oscillator, frequency conversion has been shown.<sup>4</sup> Another innovative design attempted to “stack” optical transitions within each QC active region for a so-called “cascaded” QC laser.<sup>5</sup> While this attempt had been unsuccessful in achieving simultaneous lasing from both stacked transitions, such a laser would be of interest for cascaded optical transitions capable of producing correlated photons,<sup>6</sup> which are useful in a variety of applications.<sup>7</sup> A similar concept of stacked transitions was used to demonstrate a terahertz QC laser that used electric field to select between two different wavelengths.<sup>8</sup> A semiconductor laser with an intersubband transition optically cascaded with an interband transition has been proposed,<sup>9</sup> and cascaded emission has been demonstrated in other non-QC laser systems.<sup>10</sup> Here, we report a dual-wavelength QC laser that shows simultaneous lasing from two cascaded optical transitions in its active regions.

In the two-well active region laser presented here, we take the approach of using a second-excited state from one of the active region constituent quantum wells as the upper energy state of the first optical transition (state 5 in Fig. 1). The lower energy state of the first optical transition (state 4) is a first-excited state from one of the constituent quantum wells of the active region. This same state is also the upper state of the lower optical transition, making the two optical transitions cascaded. The lowest energy state of the stacked optical transitions (state 2) is an active region constituent quantum well ground state. In the context of this specific QC laser description, we refer to a “ground state” as any state that originated from the true ground state of a constituent quantum well and accordingly for the excited states.

Our laser was grown using  $\text{In}_{0.53}\text{Ga}_{0.47}\text{As}/\text{In}_{0.52}\text{Al}_{0.48}\text{As}$  quantum wells with gas-source molecular beam epitaxy on a low-doped ( $n < 2 \times 10^{17} \text{ cm}^{-3}$ )  $\text{InP:S}$  substrate. Forty active-injector periods were used for the active core, and the design included  $0.55 \mu\text{m}$  of  $\text{InGaAs}$  ( $n = 5 \times 10^{16} \text{ cm}^{-3}$ ) cladding above and below the active region for enhanced confinement. A  $0.9 \mu\text{m}$   $\text{InP}$  ( $n = 5 \times 10^{16} \text{ cm}^{-3}$ ) buffer layer was grown before the bottom  $\text{InGaAs}$  cladding. After the top  $\text{InGaAs}$  cladding, additional cladding layers of  $3.9 \mu\text{m}$   $\text{InP}$  ( $n = 5 \times 10^{16} \text{ cm}^{-3}$ ) and  $1.1 \mu\text{m}$   $\text{InP}$  ( $n = 6.7 \times 10^{18} \text{ cm}^{-3}$ ) were grown, before capping the growth with  $0.06 \mu\text{m}$  of  $\text{InGaAs}$  ( $n = 2 \times 10^{19} \text{ cm}^{-3}$ ). Following growth, we postcalibrated our structure by measuring active region and cladding layer thicknesses with scanning electron microscopy. We found our  $\text{InAlAs}$  growth rate to be slow by 20%, and we have compensated for the difference in our design and simulations. The as-grown band structure is shown in Fig. 1. Lasers were processed as deep-etched ridge waveguides with stripe widths ranging from 9 to  $15 \mu\text{m}$  by conventional photolithography and wet chemical etching, and were electrically insulated by  $0.3 \mu\text{m}$  thick  $\text{SiN}_x$ . After evaporation of a  $\text{Ti/Au}$  (30 nm/300 nm) top contact, the sample was thinned

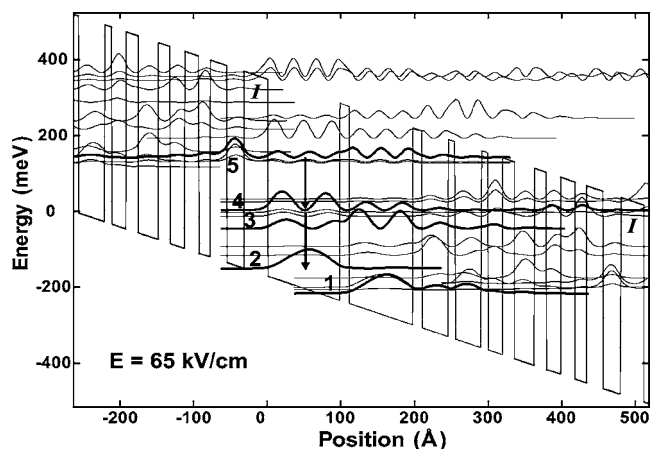


FIG. 1. Conduction band diagram for the postcalibrated layer sequence. Cascaded optical transitions are between levels  $5 \rightarrow 4$  and  $4 \rightarrow 2$ . The single stage layer sequence is (in angstroms starting from the injection barrier) **32/98/13/86/13/35/10/35/10/20/16/27/16/20/19/16/23/23**, where  $\text{In}_{0.52}\text{Al}_{0.48}\text{As}$  barrier layers are in bold,  $\text{In}_{0.53}\text{Ga}_{0.47}\text{As}$  well layers are in normal font, and Si-doped ( $2 \times 10^{17} \text{ cm}^{-3}$ ) layers are underlined. The injection barrier is labeled as *I*.

<sup>a)</sup>Electronic mail: kfranz@princeton.edu

<sup>b)</sup>Present address: Department of Electrical Engineering and Computer Science and Department of Physics, University of Michigan, Ann Arbor, MI 48109.

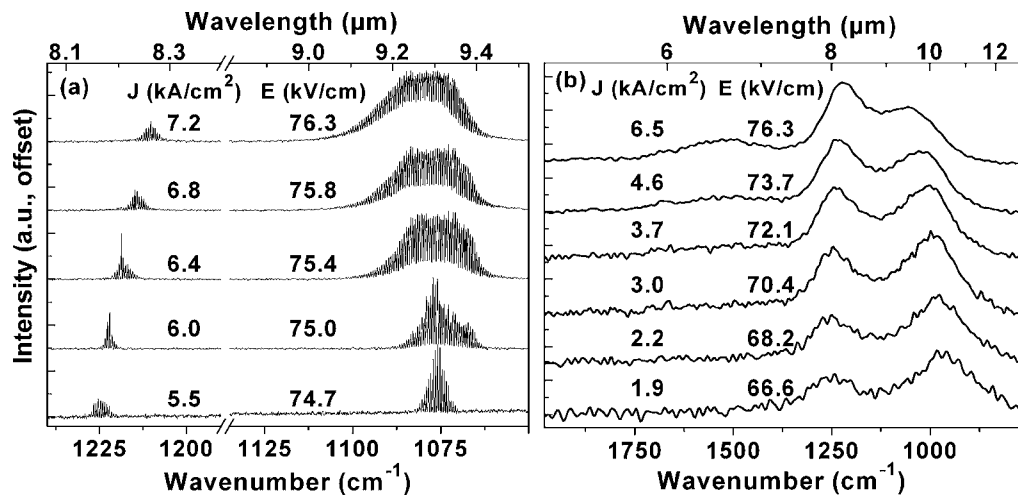


FIG. 2. (a) Emission spectra of a 2.5 mm long and 10  $\mu\text{m}$  wide laser at a heat sink temperature of 80 K operated with a 47 ns current pulse width. The electric field across the active laser core is calculated from current-voltage measurements. (b) Electroluminescence spectra from a 0.027 mm<sup>2</sup> deep-etched semicircular mesa at various current and electric field values. Electroluminescence data were collected at 80 K with a 100 ns current pulse width.

to  $\sim 200 \mu\text{m}$  and the back Ge/Au (30 nm/300 nm) contact was deposited. Laser bars were cleaved, mounted epilayer up on a Cu heat sink with In solder, and wire bonded.

Simulation for the postcalibrated structure with a 65 kV/cm applied electric field results in an energy of 128.0 meV ( $\lambda=9.68 \mu\text{m}$ ) for the upper optical transition (levels  $5 \rightarrow 4$ ) and an optical dipole matrix element of  $z_{54}=31.0 \text{ \AA}$ ; we calculate an energy of 151.5 meV ( $\lambda=8.18 \mu\text{m}$ ) for the lower optical transition ( $4 \rightarrow 2$ ) and an optical dipole matrix element of  $z_{42}=14.4 \text{ \AA}$ . The waveguide loss is estimated at  $7.4 \text{ cm}^{-1}$  for  $\lambda=9.68 \mu\text{m}$  and  $5.1 \text{ cm}^{-1}$  for  $\lambda=8.18 \mu\text{m}$ . The optical confinement factors for the active core are 60% and 67% for the two wavelengths, respectively. Considering longitudinal optical (LO) phonon scattering as the only scattering process, we calculate lifetimes  $\tau_i$  of state  $i$  as  $\tau_5=3.7 \text{ ps}$ ,  $\tau_4=1.8 \text{ ps}$ , and  $\tau_2=3.7 \text{ ps}$ .

Figure 2(a) shows time-integrated laser spectra collected using a Fourier transform infrared spectrometer. Spectra were taken using a current pulse width of 47 ns. The figure shows two distinct lasing peaks at  $\lambda \sim 9.3 \mu\text{m}$  and  $\lambda \sim 8.2 \mu\text{m}$ , in agreement with simulation for the transitions  $5 \rightarrow 4$  and  $4 \rightarrow 2$ . With increasing electric field, the spectral

distance between the two lasing wavelengths narrows. Electroluminescence (EL) data exhibit similar characteristics. Deep, wet-etched, round mesas were patterned and processed, then cleaved into semicircular structures to reduce optical feedback. The EL spectra—shown in Fig. 2(b)—exhibit two strong optical transitions that correspond to the two lasing wavelengths, and the peak centers show the same electric field tuning behavior as the laser devices. Fitting multiple Lorentzians for the 68 kV/cm spectrum gives full widths at half maximum of 18.7 meV for  $\sim 9.5 \mu\text{m}$  light and 16.2 meV for  $\sim 8.2 \mu\text{m}$  light. We note that state 5 extends over several interfaces, which can account for the broader  $5 \rightarrow 4$  transition. Simulated electric field behavior of our structure is consistent with the observed data. The open circles in Fig. 3 represent multipeak Lorentzian fits from EL data as in Fig. 2(b). Squares depict simulated energies of four possible transitions. As expected, the  $\sim 9.5 \mu\text{m}$  light results from transition  $5 \rightarrow 4$ . Because both the field behavior and energies of the  $5 \rightarrow 3$  and  $3 \rightarrow 1$  transitions differ from the EL and laser spectra, we rule out these two transitions as the source of the  $\sim 8.2 \mu\text{m}$  light. We thus determine that the

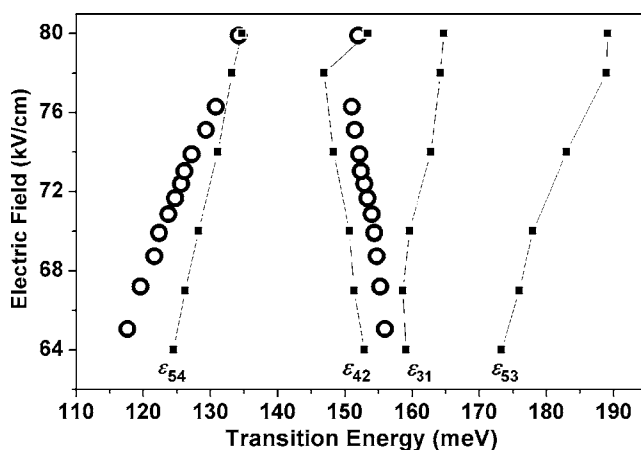


FIG. 3. Measured and calculated values of the optical transition energies in EL as a function of the electric field. Hollow circles represent the center points of multi-Lorentzian fits to the EL data as displayed in Fig. 2(b). Solid squares show the calculated transition energies.

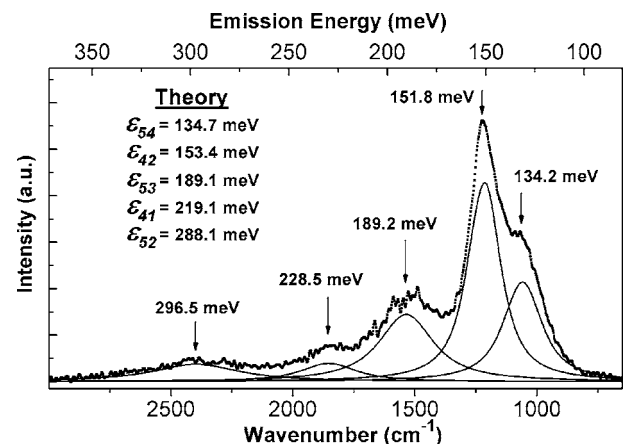


FIG. 4. Electroluminescence spectrum at 2.5 A and 80 kV/cm without correction for detector responsivity or oscillator strength. The raw data are fitted with five Lorentzian peaks, with center points indicated by arrows. Theoretical calculations are given for an electric field of 80 kV/cm and are in excellent agreement with the data.

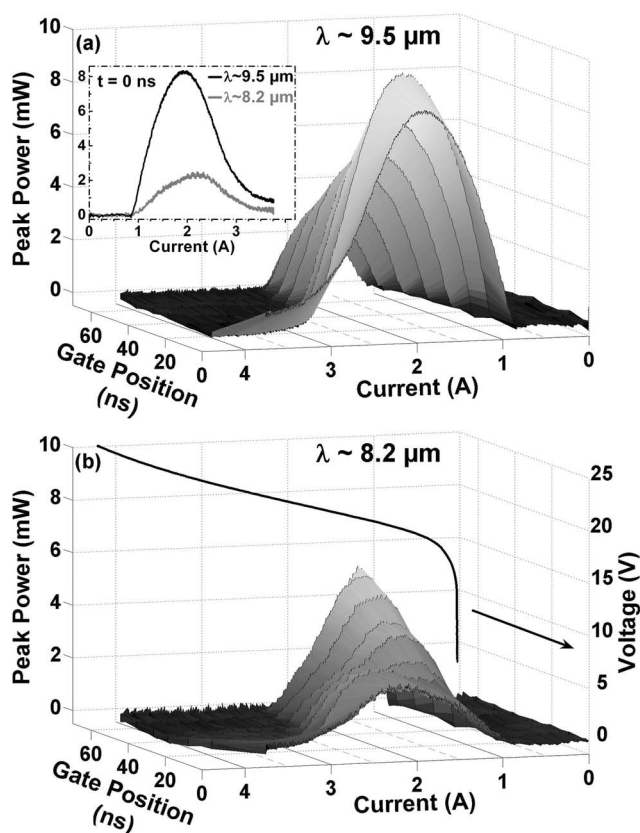


FIG. 5. Gated light vs current characteristics for (a)  $\lambda \sim 9.5 \mu\text{m}$  and (b)  $\lambda \sim 8.2 \mu\text{m}$  emissions from a 1.52 mm long,  $12 \mu\text{m}$  wide laser. Using a 14 ns boxcar gate, data were collected from different regions of an 80 ns current pulse. The leading edge of the boxcar gate was positioned at 0, 10, 20, 30, 40 50, 60, and 66 ns into the pulse, and a long pass filter with cutoff at  $8.6 \mu\text{m}$  was used to discriminate between  $\sim 8.2$  and  $\sim 9.5 \mu\text{m}$  light. The inset in (a) shows light vs current data for the  $t=0$  ns gate. The “40 ns” current vs voltage curve is shown in (b).

transition  $4 \rightarrow 2$  is the source of the  $\sim 8.2 \mu\text{m}$  light. At a current of 2.5 A (80 kV/cm), we observe five EL peaks, shown in Fig. 4. We find excellent agreement between observed and simulated data.

Figure 5 displays a series of spectrally discriminate light-current-voltage (LIV) data where a boxcar gate is used to examine 14 ns portions of an 80 ns current pulse. At the leading edge of the current pulse, the two laser thresholds have similar magnitudes. As the current pulse progresses, the  $\sim 8.2 \mu\text{m}$  light shows an increasing slope efficiency, and eventually overtakes the  $\sim 9.5 \mu\text{m}$  light in power. Also as the pulse progresses, the device must be pumped harder to turn on the  $\sim 9.5 \mu\text{m}$  light, while the threshold for  $\sim 8.2 \mu\text{m}$  light remains relatively constant throughout the pulse. The trend of less powerful  $\sim 9.5 \mu\text{m}$  light relative to the  $\sim 8.2 \mu\text{m}$  light is seen both with increasing pulse width (or gate position) and increasing temperature, suggesting the behavior is thermally induced. Phonon scattering is temperature dependent, with lifetimes decreasing as the temperature increases.<sup>1</sup> While carriers are injected into state 5 by resonant tunneling, the population of state 4 is more thermally dependent since nonradiative phonon scattering contributes to the state 4 population. Thus level 4 populates more rapidly with in-

creasing temperature, effectively reducing population inversion for the  $5 \rightarrow 4$  transition while increasing inversion for the  $4 \rightarrow 2$  transition.

That population inversion can occur for the  $4 \rightarrow 2$  transition may not be immediately obvious. Indeed, if one calculates state lifetimes based only on nonradiative scattering by LO phonons,<sup>11</sup> we find that population inversion is not established. In our structure, however, we have circumstances similar to those reported in Ref. 12, where local population inversion in  $k$  space is achieved for a single quantum well active region, while global population inversion is not necessary for lasing. When an electron nonradiatively scatters from an upper energy band to a lower band, momentum transfer dictates that it must undergo a series of additional nonradiative transitions before it affects population inversion for the optical transition. For the  $4 \rightarrow 2$  transition in our device, an electron that nonradiatively scatters to state 2 must scatter at least three more times before it affects the  $4 \rightarrow 2$  local population inversion for the optical transition. As in Ref. 12, there are also many injector states near state 2 into which electrons higher in the band can tunnel; thus  $4 \rightarrow 2$  population inversion at the laser transition is also made possible by the emptying of state 2 through tunneling.

In conclusion, we have presented a dual-wavelength ( $\sim 9.5$  and  $\sim 8.2 \mu\text{m}$ ) QC laser that exhibits simultaneous emission from two cascaded optical transitions in each active region. Future research will probe the possibility of correlated photons in a QC structure further optimized for such behavior.

This work was supported in part by DARPA-LPAS and MIRTHE (NSF-ERC). One of the authors (K.J.F.) gratefully acknowledges the support of the National Science Foundation Graduate Research Fellowship Program.

<sup>1</sup>C. Gmachl, F. Capasso, D. L. Sivco, and A. Y. Cho, Rep. Prog. Phys. **64**, 1533 (2001).

<sup>2</sup>J. Faist, F. Capasso, D. L. Sivco, C. Sirtori, A. L. Hutchinson, and A. Y. Cho, Science **264**, 553 (1994).

<sup>3</sup>A. Tredicucci, C. Gmachl, F. Capasso, D. L. Sivco, A. L. Hutchinson, and A. Y. Cho, Nature (London) **396**, 350 (1998).

<sup>4</sup>M. Troccoli, A. Belyanin, F. Capasso, E. Cubukcu, D. L. Sivco, and A. Y. Cho, Nature (London) **433**, 845 (2005); O. Malis, A. Belyanin, D. L. Sivco, J. Chen, A. M. Sergent, C. Gmachl, and A. Y. Cho, Electron. Lett. **40**, 1586 (2004).

<sup>5</sup>C. Sirtori, A. Tredicucci, F. Capasso, J. Faist, D. L. Sivco, A. L. Hutchinson, and A. Y. Cho, Opt. Lett. **23**, 463 (1998).

<sup>6</sup>M. O. Scully, Phys. Rev. Lett. **55**, 2802 (1985).

<sup>7</sup>M. Aspelmeier, H. R. Bohm, T. Gyatso, T. Jennewein, R. Kaltenbaek, M. Lindenthal, G. Molina-Terriza, A. Poppe, K. Resch, M. Taraba, R. Ursin, P. Walther, and A. Zeilinger, Science **301**, 621 (2003); A. Muthukrishnan, M. O. Scully, and M. S. Zubairy, J. Opt. B: Quantum Semiclassical Opt. **6**, S575 (2004).

<sup>8</sup>G. Scalari, C. Walther, J. Faist, H. Beere, and D. Ritchie, Appl. Phys. Lett. **88**, 141102 (2006).

<sup>9</sup>A. A. Belyanin, F. Capasso, V. V. Kocharovskiy, V. V. Kocharovskiy, and M. O. Scully, Phys. Rev. A **63**, 053803 (2001).

<sup>10</sup>H. J. G. A. P. V. Goedertier, Appl. Phys. Lett. **4**, 20 (1964); C. Santori, D. Fattal, J. Vuckovic, G. S. Solomon, and Y. Yamamoto, Nature (London) **419**, 594 (2002).

<sup>11</sup>R. Ferreira and G. Bastard, Phys. Rev. B **40**, 1074 (1989).

<sup>12</sup>J. Faist, F. Capasso, C. Sirtori, D. L. Sivco, A. L. Hutchinson, M. S. Hybertsen, and A. Y. Cho, Phys. Rev. Lett. **76**, 411 (1996).